Volume 7
Number 2
26 January 2026
Pages 667–1330

Materials Advances

rsc.li/materials-advances

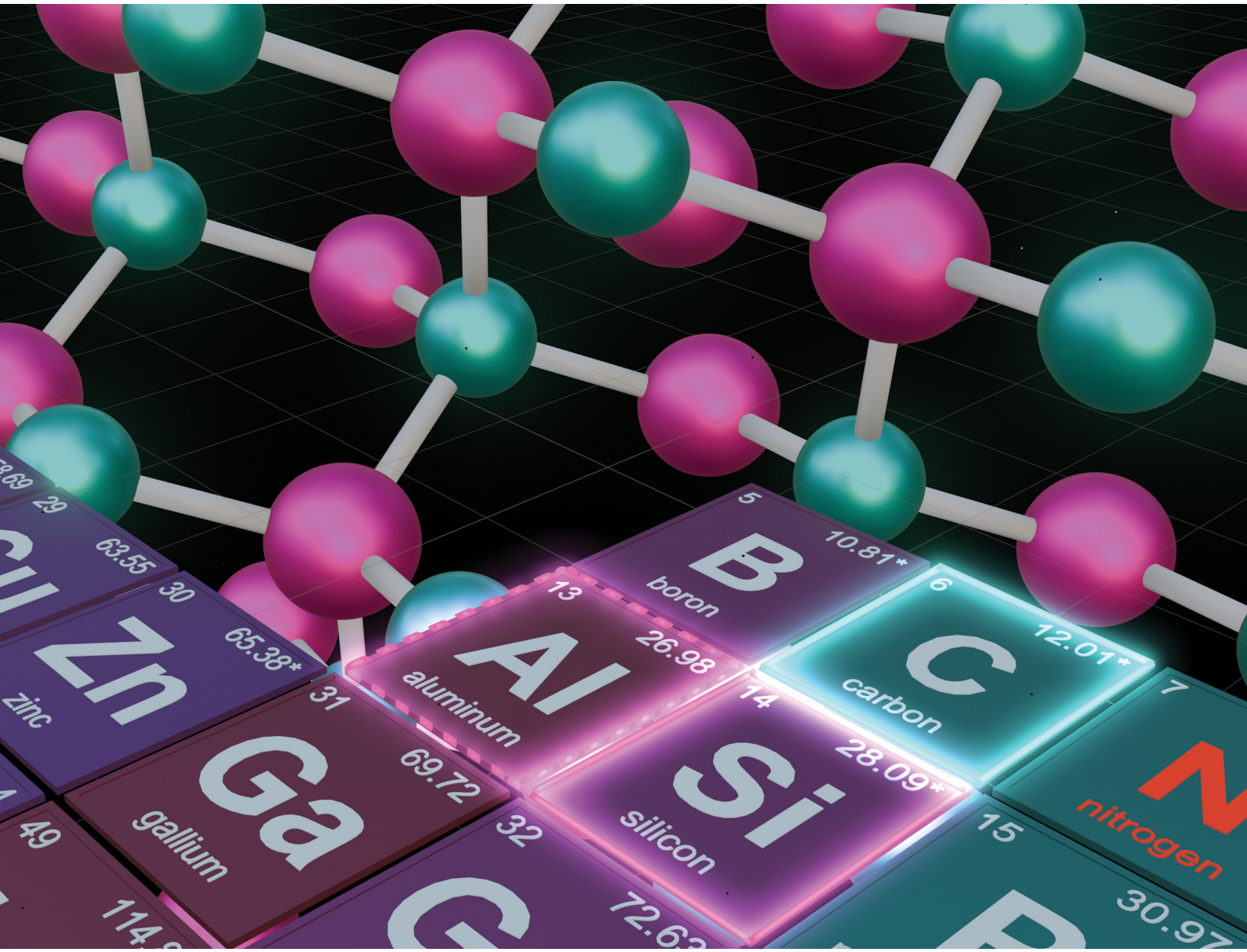

ISSN 2633-5409

ROYAL SOCIETY OF CHEMISTRY

PAPER
Adam Gali, David Beke *et al.*
The role of aluminum in controlling defect formation and polytypism in silicon carbide *via* thermal synthesis

Materials Advances

ROYAL SOCIETY OF CHEMISTRY

PAPER

View Article Online
View Journal | View Issue

Cite this: *Mater. Adv.*, 2026, 7, 783

The role of aluminum in controlling defect formation and polytypism in silicon carbide *via* thermal synthesis

Sarah Morais Bezerra,[ab] Sándor Kollarics,[acd] Luisa Souza Almeida,[e] Gábor Bortel,[a] Nikoletta Jegenyés,[a] Bence Gábor Márkus,[af] Ferenc Simon,[adf] Adam Gali*[agh] and David Beke*[ai]

The synthesis of silicon carbide has been widely explored to tailor its material properties for specific needs, particularly particle size, polytype distribution, and defect density. While many applications require defect-free material, the intrinsic defect states in SiC make it an attractive candidate for quantum technologies. However, the controlled introduction of such defects remains a major challenge. In this work, we investigate the influence of aluminium concentration and high-energy ball milling duration on defect formation and polytype distribution in silicon carbide synthesized through controlled thermal reactions. Our findings highlight the critical role of Al in altering the reaction between Si and C, stabilizing specific polytypes, and promoting the formation of optically and magnetically active point defects. Multivariate analysis using machine learning-assisted partial least squares regression revealed strong correlations between structural parameters and defect concentrations. These results demonstrate that optimizing Al concentration and milling conditions enables controlled synthesis of SiC with tailored polytypism and targeted defect configurations, presenting a scalable route for quantum technological applications.

Received 14th July 2025,
Accepted 17th November 2025

DOI: 10.1039/d5ma00751h

rsc.li/materials-advances

1. Introduction

Silicon carbide (SiC) is a polymorphic material that can crystallize in more than 200 distinct polytypes,[1–4] which differ in the stacking sequence of their Si–C bilayers along the crystallographic *c*-axis. The most common are the cubic 3C-SiC (β-SiC) and the hexagonal 4H- and 6H-SiC (α-SiC) polytypes. These structural variations result in differences in their electronic and optical properties, making polytype control crucial for tailoring material performance in electronic and quantum applications.[5] The synthesis of silicon carbide has therefore been extensively studied, primarily with the aim of obtaining crystals with minimal defect densities and controlled polytype compositions.[2–4,6] Initial studies by Knippenberg[7] and Inomata *et al.*[8] suggested that temperature is a critical parameter influencing polytype formation, reporting that the cubic polytype (3C-SiC) predominantly forms at lower temperatures, while hexagonal polytypes (4H- and 6H-SiC) form at higher temperatures. Subsequent research confirmed the influence of temperature but indicated that it is not the sole determinant of polytype distribution.[9–11]

The principal industrial methods for synthesizing SiC include the Acheson process,[12,13] the Lely method,[14] and chemical vapor deposition (CVD).[15] Each technique has unique strengths and limitations. The Acheson process, widely established in industry, enables large-scale production but offers limited control over polytype purity, defect concentration, and particle morphology. In contrast, CVD achieves high-quality SiC crystals but is costly and produces limited quantities per cycle. Consequently, alternative synthesis methods have been explored to tailor SiC properties for specific applications, such as precise particle size control,[16] defect minimalization,[17] and thin film deposition.[18]

[a] *HUN-REN Wigner Research Centre for Physics, Institute for Solid State Physics and Optics, P.O. Box 49, H-1525 Budapest, Hungary. E-mail: gali.adam@wigner.hun-ren.hu, beke.david@wigner.hun-ren.hu*
[b] *Department of Physical Chemistry and Materials Science, Faculty of Chemical Technology and Biotechnology, Budapest University of Technology and Economics, Műegyetem rakpart 3, H-1111 Budapest, Hungary*
[c] *SOLEIL Synchrotron, L'Orme des Merisiers, RD128, Saint Aubin, 91190, France*
[d] *Department of Physics, Institute of Physics, Budapest University of Technology and Economics, Müegyetem rakpart 3, H-1111 Budapest, Hungary*
[e] *São Carlos Institute of Chemistry, University of São Paulo, 13566-590 São Carlos, Brazil*
[f] *Stavropoulos Center for Complex Quantum Matter, Department of Physics and Astronomy, University of Notre Dame, Notre Dame, IN 46556, USA*
[g] *Department of Atomic Physics, Institute of Physics, Budapest University of Technology and Economics, Müegyetem rakpart 3, H-1111 Budapest, Hungary*
[h] *MTA-WFK Lendület "Momentum" Semiconductor Nanostructures Research Group, P.O. Box 49, H-1525 Budapest, Hungary*
[i] *Kandó Kálmán Faculty of Electrical Engineering, Óbuda University, Tavaszmező. 17, H-1084 Budapest, Hungary*

Typically, SiC synthesis from elemental silicon and carbon occurs through combustion or analogous reaction methods.[19,20] Alternatively, conventional thermal synthesis offers enhanced control by allowing a gradual temperature increase,[21] thereby promoting homogeneous particle formation compared to combustion synthesis.[22] Controlled methodologies have enabled the systematic investigation of factors influencing polytype stabilization. Notably, certain precursor additives have been identified as stabilizing agents for specific polytypes.[23] Nitrogen and phosphorus generally stabilize the cubic polytype, whereas aluminum favors hexagonal polytypes.[24]

In other words, additives incorporated into the reaction mixture function as promoters, often effectively reducing the reaction temperature, modulating the reaction conditions, and potentially favoring specific polytype formation without elevating impurity levels in the final product. For instance, a reported 60 : 20 Al to Si ratio has been shown to yield high-purity silicon carbide with no detectable aluminum contamination.[25]

Indeed, the formation energies across SiC polytypes exhibit minimal variation, suggesting that polytype distribution is influenced by factors beyond energetic considerations alone.[1] Rajabzadeh *et al.* attributed the stabilization effects to differences in valence and conduction band alignments among polytypes.[26] Their calculations revealed that nitrogen doping raises the Fermi level to the conduction band, reducing the bandgap, whereas aluminum doping lowers the Fermi level to the valence band.

Introducing additives in the precursor mixture to stabilize polytypes also increases the likelihood of stacking faults and associated defects.[26] These defects adversely impact SiC performance by reducing carrier lifetime, deteriorating mechanical properties, and increasing electrical leakage currents and device on-resistance, ultimately compromising device reliability.[27]

Despite such defects often being considered undesirable, recent research has explored their beneficial properties, analogous to those of nitrogen-vacancy (NV^-) centers in diamond.[28–31] Specific defects in SiC, such as carbon antisite vacancies (CAVs) and negatively charged silicon vacancies (V_{Si}^-), exhibit promise as single-photon emitters[32] and qubits exhibiting spin coherence at room temperature,[5,33–38] respectively, which makes SiC ideal for quantum information processing[39] and sensing applications.[40] Compared to diamond, SiC offers advantages such as reduced production costs and a broader range of defect structures due to its polytypism.[41–45] However, traditional defect creation techniques using irradiation or implantation are complex, expensive, and typically yield low defect densities.[46–52]

In this study, we employed a controlled tube furnace synthesis method, leveraging an aluminum additive in the reaction mixture to enhance stacking fault formation and promote defect generation tailored for quantum technological applications. Our findings indicate that the amount of Al used in the precursor has a significant influence on the formation mechanism of silicon carbide. Without Al, the cubic polytype is the dominant phase, accompanied by a decrease in defect density. Conversely, moderate Al concentrations in the precursor promote the formation of hexagonal polytypes and increase the concentration of point defects in the synthesized SiC. Interestingly, higher Al concentrations (20 mol%) in the precursor lead to increased formation of cubic polytypes with a lower defect density, which contradicts initial expectations. Furthermore, using chemometrics techniques – which rely on statistical and machine learning models to extract meaningful patterns from complex datasets – we reveal direct correlations among crystallite size, polytype distribution, and defect density. This data-driven approach enabled us to uncover subtle interdependencies that are not readily apparent through conventional analysis, highlighting the potential of artificial intelligence-assisted methods in the study of structure–defect relationships. We propose a reaction mechanism involving aluminum–carbon interactions that explains the observed variations in polytype distribution and defect density. Based on these insights, we recommend specific synthetic approaches for tailoring desired defect concentrations in SiC for targeted quantum technological applications.

2. Methodology

Silicon (Si) powder ($\sim$325 mesh, 99% trace metals basis, Sigma-Aldrich), activated carbon (C, NORIT® A SUPRA EUR USP, Sigma-Aldrich), poly(tetrafluoroethylene) (PTFE, powder, 1 μm particle size), and aluminum (Al, powder, $\geq$91% complexometric) were used as raw materials. The powders were loaded into high-energy ball milling equipment (Planetary Micro Mill, PULVERISETTE 7, FRITSCH) with varying molar fractions of Al (0%, 5%, 10%, and 20%). The ball-to-powder ratio (BPR) was maintained at 1 : 10, and the milling speed was set to 500 rpm.

To control the temperature and prevent excessive heating, the milling process was performed in cycles of 10 minutes of milling followed by a 5-minute rest period, as established in preliminary tests. The temperature increase during a 5-minute cycle was about 20 °C (from 25 °C to 45–47 °C). Isopropanol was used as a milling medium to minimize particle agglomeration and maintain a uniform, oil-like consistency in the sample. Additionally, the milling was conducted under an argon atmosphere to prevent oxidation. The total milling durations were set at 1, 2, 3, and 4 hours to investigate the effect of processing time on the final material properties.

The milled powder samples were pressed into 20 mm diameter pellets to enhance the interaction between reagents. A 5 w/w% polyvinyl alcohol (PVA) solution was added dropwise to the powder, followed by mixing and weighing 1.5 g of material for each pellet. The pellets were then compacted under 7 tonnes and dried overnight to remove residual moisture. Silicon-carbide nanoparticles (SiC NPs) were synthesized using a Carbolite (CTF 18/–/300) tube furnace with a temperature ramp rate of 5 °C min^{-1} under an argon (UHP/5.0) atmosphere. The thermal treatment process involved an initial dwell at 200 °C for 60 minutes, followed by a second dwell at 1250 °C for an additional 60 minutes. After cooling, the samples were weighed and subjected to secondary heat treatment at 650 °C for 10 hours in air to remove unreacted carbon. To eliminate

residual silicon and remove aluminium, the samples were etched overnight in a $HF:HNO_3:H_2O$ (1 : 1 : 10) solution. Finally, the product was thoroughly washed with deionized water until the pH stabilized at 5. This procedure was generally effective;[53–58] however, in some cases, traces of Si and Al_2O_3 persisted after etching. Importantly, the concentrations of these residual species did not correlate with milling duration or the initial aluminium content in the precursor, and varied randomly across repeated experiments (0.5–7 at% Al). Although additional etching cycles further reduced their presence, no measurable influence of these residues on the experimental data was detected. Therefore, to minimize potential surface modifications—since the acidic solution can alter the SiC surface chemistry[57] and affect both EPR and Raman responses—all samples were characterized after a single standard etching step. The incomplete removal of Si and Al is attributed to differences in particle morphology and surface topology, which may locally hinder reagent access and limit leaching efficiency.

Samples were subsequently labeled based on milling duration and aluminum additive concentration. However, it is important to note that the latter parameter does not reflect the aluminum concentration within the final product. The incorporation of aluminum into the precursor mixture influences the reaction mechanism and, consequently, the properties of the synthesized SiC. Due to the limited solubility of aluminum, it predominantly forms a separate phase, which was removed during the purification process. Further details and discussion can be found in the subsequent sections.

Powder X-ray diffraction (XRD) measurements were performed using a Huber G670 Guinier Imaging Plate Camera with Cu $K\alpha_1$ radiation (λ = 1.5406 Å). The samples were enclosed in special glass capillaries (Mark-tubes made of special glass, WJM-Glas Müller GmbH) with a diameter of 0.5 mm and a wall thickness of 0.01 mm, ensuring proper containment and minimizing background interference. Rietveld refinement was performed using Topas Academic to characterize the polytype formation and crystallite size.

Scanning electron microscopy (SEM) was conducted using a TESCAN MIRA3 electron microscope. For sample preparation, the material was dispersed in water and subjected to ultrasonication for 30 minutes to ensure a homogeneous distribution. The resulting suspension was then drop-cast onto silicon wafer and allowed to dry before imaging.

EPR measurements were performed using a Magnettech MiniScope MS-400 X-band spectrometer equipped with a TE_{102} rectangular resonator. The magnetic field was swept from 331 to 341 mT (9.38 GHz, 0.1 mT modulation amplitude, and a MW power of 10 mW). The EasySpin[59] Toolbox was used to obtain fits on the experimental data.

Raman measurements were performed using a Renishaw inVia confocal Raman microscope equipped with a 532 nm excitation laser and 1800 lines per mm gratings. For the fitting, Voigt functions were used in OriginPro 2025 software from OriginLab Corporation, Northampton, MA, USA.

Photoluminescence measurements were conducted using a QE-Pro spectrometer (Ocean Optics, Ocean Insight, USA). An integrating sphere (819C-IS-5.3, Newport, USA), in conjunction with a collimator and a 550 nm long-pass filter (FEL0550, Thorlabs), was employed to enhance the measurement accuracy. The laser used to excite the samples was a 520 nm (Roithner Lasertechnik GmbH, RLTMDL-520-1W-05) CW laser. The photoluminescence peaks were deconvoluted using OriginPro 2025.

All measurements were performed at room temperature.

Statistical methods: principal component analysis (PCA) was used as exploratory analysis, and partial least squares (PLS) was used for calibration analysis using MATLAB 2022b software with the PCA toolbox and Regression toolbox 1.4.[60,61] PCA was calculated with 3 principal components (PCs), and the data were mean-centered. In PLS 3, latent variables (LVs) were used. The validation was done by contiguous blocks cross-validation. The use of machine learning (ML), a well-established branch of artificial intelligence (AI), involves the calculation of statistical models learning through examples instead of preprogrammed rules.[62,63] When applied to chemometrics, the area of chemistry that studies how to better extract chemically relevant information from data produced in chemical experiments, it is easier to find patterns and correlate information on multivariate data.[64]

3. Results and discussion

SEM imaging confirmed the formation of silicon carbide nanoparticles (SiC NPs) with a range of shapes and sizes (Fig. 1). In samples synthesized from aluminum-containing precursors, the presence of both spherical particles and well-defined, faceted structures was observed. In contrast, samples synthesized without aluminum exhibited whisker-like morphologies, indicating distinct formation mechanisms.

It is reported[65] that SiC whiskers typically form *via* a solid–gas reaction, where a gaseous silicon-containing species ($Si_xY_y(g)$) reacts with solid carbon. In this mechanism, preferential growth occurs along the lowest-energy (111) facet, resulting in the characteristic whisker morphology. Conversely, spherical SiC structures are commonly associated with a solid-state reaction between silicon (in either liquid or solid form) and carbon (in solid form). Silicon and carbon react at around 1450 °C to form SiC.[66] Silicon begins to melt at approximately 1400 °C. However, the presence of aluminum in the precursors can lower the reaction temperature.[67,68] This may be accounted for by the morphological differences observed in samples prepared in the presence of Al.

Both XRD and Raman analyses revealed broad peaks in the samples, indicating small crystallite sizes and high defect densities. Given the polytypism and the variety of possible defect configurations across all polytypes, we employed multiple analytical approaches to evaluate the data. The resulting data were compared to gain deeper insight into the structural and electronic properties of the system. A schematic overview of the applied methodology is presented in Fig. 2, and the corresponding measured data are provided in the SI.

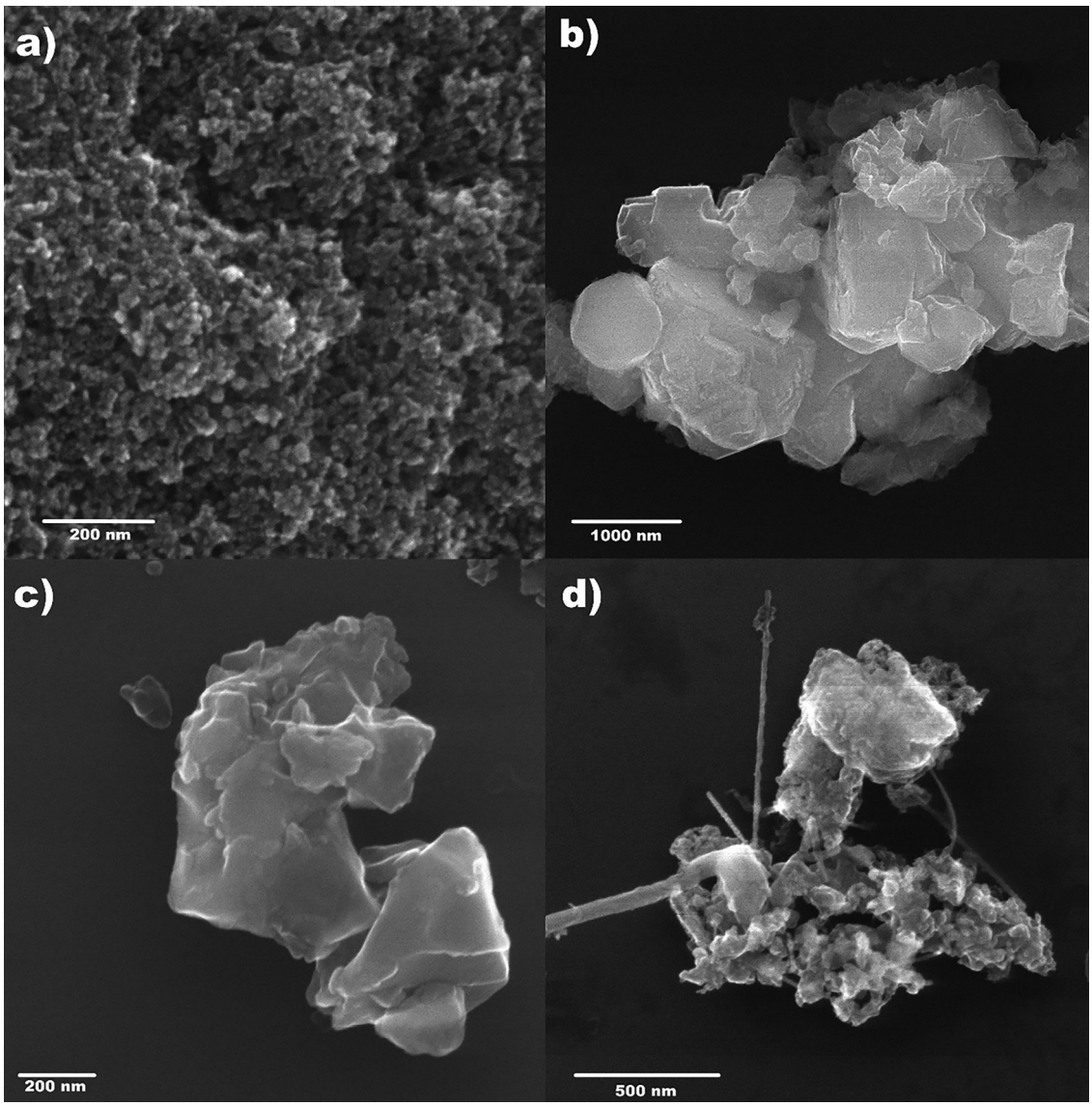

Fig. 1 SEM images of the samples with different amounts of Al in the precursors and various milling times: (a) 10%Al-0 h, (b) 20%Al-4 h, (c) 5%-0 h and (d) 0%-0 h.

The analysis of the X-ray diffractograms confirmed the presence of multiple SiC polytypes, including 3C-SiC, 6H-SiC, and 4H-SiC, with occasional detection of the rare 2H-SiC phase. The measured data, reference spectra, and analysis results are reported in the SI (Fig. S1–S4).

In samples synthesized without aluminum, the predominant polytype was cubic (3C-SiC). However, with an increase in Al concentration in the precursor, the cubic fraction decreased and then increased with an increase in Al concentration, showing a minimum at around 5–10 at% Al, as shown in Fig. 3a. The applied milling time also affected the polytype ratios (Fig. S5a). The calculated polytype ratios showed no changes in samples with 0% and 20% Al, except for a 10% fluctuation in the sample with no added Al and a 3% variation in the sample with 20% Al in the precursor. In samples with 5% Al in the precursor, the hexagonal-to-cubic ratio displayed an overall decrease with some fluctuations in milling time, while samples with 10% Al in the precursor exhibited an increase in cubic SiC concentration.

Crystallite size (Fig. 3b) also followed a concave trend with an increase in Al concentration in the precursor but remained mostly unaffected by milling time (Fig. S5b). This correlation between 3C-SiC formation and crystallite size suggests that an increase in hexagonal polytypes is associated with a reduction in overall crystallite size.

Similar trends have been reported in previous studies: the Al content influences the microstructure: low Al precursor concentrations, such as 5 at%, favor the formation of fine, interconnected grains and robust porous monoliths,[69] consistent with our SEM and XRD results. Conversely, higher Al precursor concentrations (*e.g.*, 20 at%) result in larger crystals due to the increased formation of a thicker, more mobile Al–Si liquid/

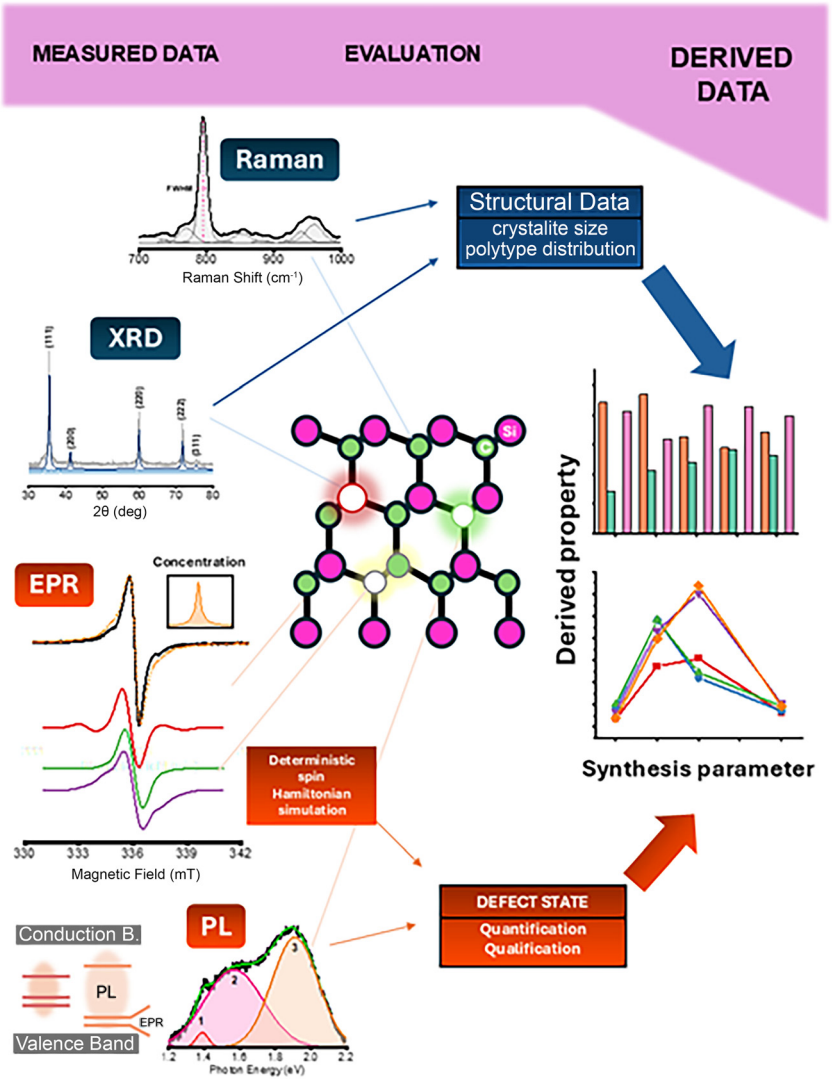

Fig. 2 Schematic overview of the data analysis workflow. The evaluation combines structural and spectroscopic methods to characterize polytypic and defect-rich samples.

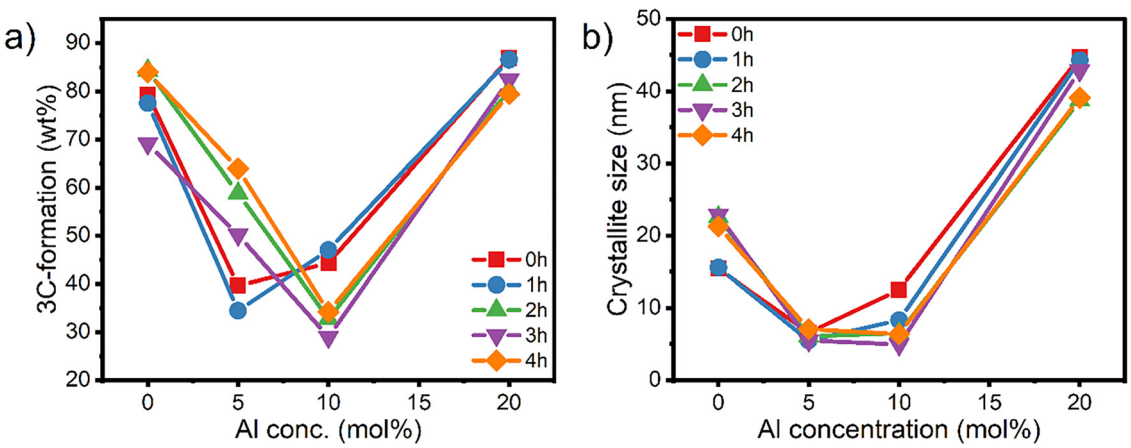

Fig. 3 (a) 3C-SiC formation and (b) crystallite size as a function of Al concentration in the precursor.

vapor phase, elevating surface diffusion, supersaturation-driven 2D nucleation, and Ostwald ripening processes,[70] as observed in our study.

X-ray diffraction primarily detects long-range, averaged crystal structures, providing information on phase composition, lattice parameters, and overall crystallinity. However, minor variations in these parameters result in subtle changes in the XRD pattern. In contrast, Raman spectroscopy probes the vibrational modes of chemical bonds within the crystal lattice. These vibrational signatures are overly sensitive to local structural variations, including different SiC polytypes, defects, strain, doping, and slight compositional changes, that can induce broadening, peak shifts, or splitting in the Raman spectrum, making it more responsive to subtle structural variations.[71,72]

The longitudinal optical mode (LO) and transverse optical mode (TO) Raman bands of the synthesized SiC exhibited variations in shape depending on milling time and Al concentration in the precursor (Fig. S6). The Raman spectra of the samples synthesized without the presence of Al in the precursor, and somewhat the samples made with 20% of Al, resembled those of 3C-SiC, and these results corroborate their XRD patterns. The most notable differences among the samples were the variation in the LO-to-TO peak ratio and peak width, as well as the presence of broad peaks on the left side of the LO and TO peaks. In some cases, these red-shifted peaks dominated the spectra.

The Raman spectra of samples made with 5% and 10% Al in the precursor were significantly broader, exhibiting numerous recognizable or unresolvable peaks in the 700–1000 cm^{-1} spectral range. This broadening correlates closely with variations in crystallite size and cubic polytype fraction derived from XRD analysis, suggesting that these structural factors significantly influence the microcrystalline environment probed by Raman spectroscopy.

Although the overall broadening is challenging to quantify precisely, assumptions can be made for SiC systems. The LO and TO of 3C-SiC are located at 790 and 940 cm^{-1}, respectively.[73] In an ideal, infinite crystal, only vibrations from the center of the Brillouin zone contribute to first-order Raman scattering ($q \approx 0$). However, short-range disorder, bond distortions, or nanocrystallinity disrupt periodicity and spatially confine phonons, introducing uncertainty in the wave vector within the Brillouin zone. As a result, in finite-sized crystals, the relaxation of Raman selection rules allows transitions with finite crystal momentum, $q \neq 0$. If the phonon dispersion curves within the first Brillouin zone are not flat, this results in band broadening and shifts. Consequently, transitions beyond the zone center become allowed.

The presence of defects also results in an increased band broadening and the emergence of spectral shoulders. Silicon carbide is known to contain defects such as twins, dislocations, and inclusions, with stacking faults being the most prevalent.[71] Stacking faults can be identified through the presence of a shoulder at approximately 768 cm^{-1}, accompanied by the broadening and softening of the TO peak. Additional factors, such as strain and surface layer effects, also influence the Raman spectra.[72,74,75] Furthermore, a broad band centered around 860 cm^{-1} has been previously observed in nanoscale SiC and is attributed to the presence of amorphous SiC,[76] or Fröhlich transitions. Here, the Fröhlich mode is due to the change in the Fröhlich-type electron–phonon interaction, as the presence of structural defects causes the relaxation of the selection rules, leading to the appearance of otherwise silent modes.[77]

Since the most abundant defects in SiC are stacking faults, it is also likely that the hexagonal SiC structures, or parts of these structures, detected by XRD, are not lone particles per se, but small inclusions within the material's structure, such as stacking faults (SFs). The proximity of SFs correlates directly with the extent of broadening and the position of the TO peak.[71,73]

To analyze these spectral features quantitatively, we employed Voigt curve fitting to extract the full width at half maximum (FWHM) and peak positions. This approach provided detailed insights into peak broadening, frequency shifts, and the potential emergence of additional polytypes within the synthesized materials. The linewidths (FWHM) of the TO peaks are plotted in Fig. 4 and Fig. S7. However, the observed linewidths were broader than the reference simulation[73] used to describe the influence of SFs on the Raman spectra. The variation of the linewidth showed a pattern similar to the hexagonal ratios obtained from XRD measurements, with the exception of the 1 h samples. Besides stacking faults, point defects also modify the Raman spectra.[78–80] The peaks at lower Raman shifts, for example, (720–730 cm^{-1}), which are also visible after fitting in most samples, can be related to the formation of defects, specifically carbon antisite defects.[81] However, neither the TO linewith nor the area around 720–730 cm^{-1} show similarities to the EPR data discussed below (Fig. S8) Although we cannot directly attribute these deviations to differences between the 1 h milled samples and others, our statistical analysis demonstrates that, despite observed similarities in the trends of hexagonality, Raman

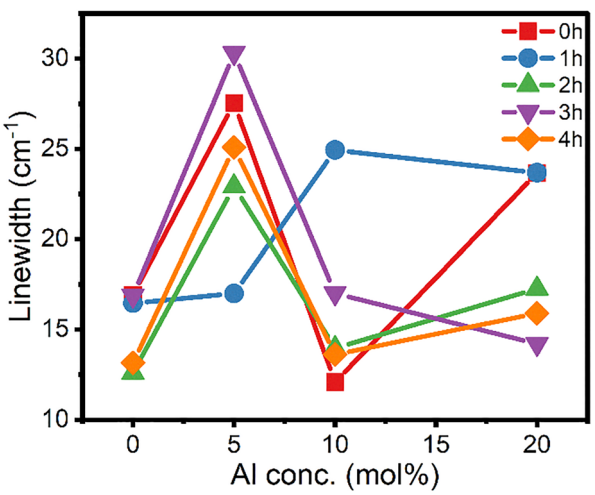

Fig. 4 Linewidth of TO peaks after fitting with a Voigt function, which correlates with SF concentration.[71,73]

linewidth, and defect concentration measured *via* EPR, there is no direct correlation between the Raman TO linewidth and the properties that are expected to influence it.

The LO band is generally utilized for the determination of free carrier densities. The interaction between the LO phonons and plasmons leads to the formation of a hybrid mode known as the LO phonon–plasmon coupled (LOPC) mode. This results in a broadening and shift of the LO peak. The change in the spectral features is proportional to the free carrier density. Thus, higher free carrier densities result in more pronounced alterations in the spectra.[82] In other words, both p-type and n-type doping can lead to the formation of LOPC modes. However, while n-type doping generally causes a noticeable hardening of the LO peak, the softening associated with p-type doping is usually less significant. Given that Al was used during the synthesis, some degree of p-type doping is expected. Nevertheless, in our samples, although the LO peaks exhibit broadening, no corresponding red shift was observed, rendering this phenomenon inapplicable to estimate carrier density in our samples; however, it excludes high variation in doping levels, regardless of the different amounts of Al used for the synthesis, consistent with the XRD results.

The shoulder on the LO peaks around 915 cm^{-1} is also thought to be related to structural defects arising from changes in the polarization selection rules and wave vector due to disordered lattices,[71,83] and they were observed in all samples. From the peaks in between the LO and TO peaks, we can assign most of them to hexagonal polytypes (4H and 6H), Fröhlich transitions, and the formation of amorphous SiC.

A notable difference is observed in the Raman spectra of samples milled for 2 hours, which exhibited significantly narrower peaks and fewer additional features, irrespective of the Al concentration in the precursor (Fig. S6). This indicates a reduction in structural disorder and improved crystallinity compared to samples subjected to other milling durations. Interestingly, XRD analysis did not reveal any corresponding differences between the two-hour milled samples and the others, despite both techniques being sensitive to structural characteristics. The better crystallinity, indicated by Raman data, suggests that two hours is an optimal milling time for SiC nanoparticles with a low amount of structural defects and amorphization.

Beyond two-dimensional structural defects, silicon carbide is also known for exhibiting point defects. Electron paramagnetic (EPR) spectroscopy can be employed as an analytical technique to excite the electronic spin between the Zeeman levels of unpaired or conducting electrons. Given that the majority of defects of interest exhibit EPR signals, this method can be utilized to both qualify and quantify these specific defects within a given structure.

To quantify the number of spins per mg concentration, we used eqn (1) from ref. 84 with omitting the "scan" factor already considered in the area of the spectra (Fig. S9).

$$[\mathrm{X}] = \frac{\mathcal{A}_\mathrm{X} G_\mathrm{std} (B_\mathrm{m})_\mathrm{std} (g_\mathrm{std})^2 [S(S+1)]_\mathrm{std} P_\mathrm{std}{}^{1/2}}{\mathcal{A}_\mathrm{std} G_\mathrm{X} (B_\mathrm{m})_\mathrm{X} g_\mathrm{X}{}^2 [S(S+1)]_\mathrm{X} P_\mathrm{X}{}^{1/2}} [\mathrm{std}]$$

where $\mathcal{A}$ is related to the area under the curve after double integration, G is the gain, B is the modulation amplitude, g is the g-factor of the sample, S is the spin state, P is the microwave power. The std notation corresponds to the used standard, and the X refers to values of the sample. The results can be found in Fig. 5a and Fig. S10, S11.

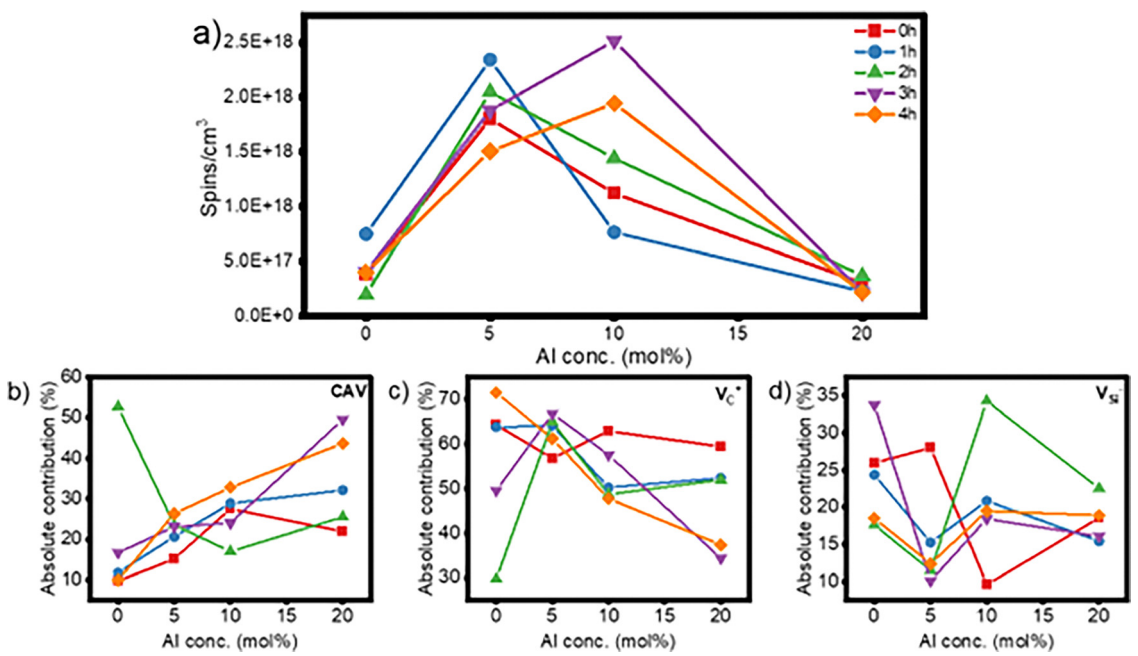

Fig. 5 (a) Calculated defect concentration as a function of Al concentration in the precursor for various milling times. The contribution of the three vacancies, (b) carbon antisite vacancy pair (CAV), (c) carbon vacancy (V_C^{+}), and (d) silicon vacancy (V_{Si}^{-}), which were used to simulate the experimental data.

The overall defect concentration exhibited a pattern consistent with the trends observed in crystallite size and cubic phase formation: samples characterized by the highest proportion of hexagonal polytypes and the smallest crystallite sizes demonstrated the greatest defect concentrations. The samples made with 10% precursor Al concentration and milled for 1 h showed some deviation from the observable trend of the defect density, similar to the observed differences in FWHM of the Raman TO mode; however, the deviation in the EPR signal was more substantial. Initially, it can be inferred that the observed defects may be associated with one or both XRD parameters. Previous studies[85,86] have linked defects predominantly to the crystallite size. Other studies have also demonstrated a correlation between the size and defect concentration in SiC nanowires,[87] and in films.[88]

To quantitatively explore the correlations among the three visually similar datasets obtained from XRD, Raman, and EPR measurements, we employed statistical methods for cross-analysis. Proceeding with a multivariate regression model helps to reduce bias in the selection of variables that are likely to have the most significant impact on the model.[89] Thereupon, this approach is used to derive a comprehensive result encompassing the whole XRD data, rather than confining the analysis to specific concentration values. PLS mathematically predicts the behavior of a sample based on a series of previous measurements taken under established conditions through the implementation of inverse calibration regression.[90] Specifically, it calibrates the analytical values (area under the EPR spectrum), denoted as Y, with the measured values, X (diffractograms).[91] Unlike univariate analyses, which consider only single-variable relationships, PLS accounts for multiple varying regions, facilitating the simultaneous analysis of how variations in defect concentration correspond to changes in the XRD spectra. Therefore, it is possible to assess the overall variation of the diffractogram and visualize this variation in a multidimensional space to identify correlations. Subsequently, it optimizes redundant information to maximize the explanatory power of the model with respect to the observed data. Hence, it is feasible to extract chemical information from the acquired data.[92]

PCA is a multivariate statistical technique utilized to reduce the dimensionality of complex datasets, such as spectroscopic measurements characterized by high amounts of variables.[93] PCA operates by orthogonally transforming the original data matrix into a set of axes known as principal components (PCs), which encapsulate the maximum variance within the data.[94] This transformation involves the calculation of eigenvectors of the covariance (or correlation) matrix. By transforming the original data into these eigenvector-defined axes, PCA simplifies subsequent analyses, facilitating the detection of data trends, outliers, and distinct patterns that may be obscured within the high-dimensional variable space.

PLS gave three latent variables, the metrics obtained, shown in Table 1, and the scores plotted in Fig. 6. These results show that the data between XRD and the area of the EPR have a good correlation.

Table 1 Results from PLS

Parameter	Value
R^2	0.926
RMSE	0.0505
R^2CV	0.697
RMSECV	0.1024
Explained variance	95%

In Table 1, R^2 denotes the coefficient of determination, indicating the goodness of fit of the model. RMSE represents the root-mean-square error of the regression, analogous to the standard deviation of residuals. R^2CV is the cross-validated coefficient of determination, while RMSECV denotes the root-mean-square error obtained from cross-validation. The explained variance (95%) indicates that the univariate measurement, specifically the EPR area, accounts for the signal's variability and demonstrates a correlation with 92% confidence. Despite the EPR measurement being less complex and providing less information, it correlates well with the XRD, which encompasses critical and more parameters such as polytype, particle size, crystallinity, among others.

To further investigate the relationship identified by PLS analysis, we conducted additional statistical analyses. A linear regression (Fig. S14) between the 3C-SiC fraction and the defect concentration yielded good negative Pearson coefficients (Table S2), indicating a statistically significant inverse relationship consistently observed across all samples: as the fraction of the cubic polytype (3C-SiC) decreases, the defect concentration increases. In contrast, neither linear regression nor Spearman's rank correlation (Fig. S15 and Tables S1–S3) revealed any statistically significant relationship between the crystallite size and defect concentration or between the crystallite size and 3C-SiC fraction when data from individual milling times were analyzed separately or combined. Also, when data from all milling times were combined (Table S4), the Spearman method did yield a statistically significant correlation between defects and 3C-formation. These analyses suggest that the variations observed in the XRD patterns, in conjunction with changes in defect concentration, are primarily governed by differences in polytype composition rather than crystallite size.

When Raman data was used as matrix X in PLS, we had R^2 = 0.722, RMSE = 0.0981, R^2CV = 0.517, and RMSECV = 0.1293, and an explained variance of 85%. However, the relatively low performance metrics, particularly those from cross-validation, suggest the absence of a statistically significant correlation between defect concentration and Raman spectral features—even though the peak at 720 cm^{-1} has been previously linked to the paramagnetic antisite vacancy.

The PLS analysis between the Raman TO linewidth (as Y), which was previously connected to the presence of SFs, and the XRD data (as X), which should show higher hexagonal fractions when the SF concentration increases, gave high explained variance (95%); however, all the statistical metrics were poor: R^2 = 0.418, RMSE = 4.06, R^2CV = −0.064, and RMSECV = 5.49.

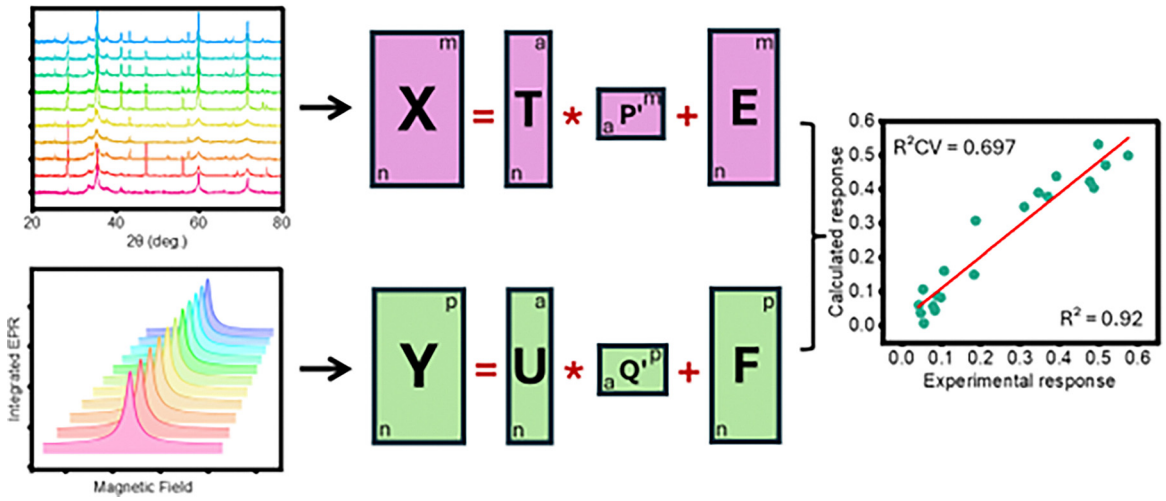

Fig. 6 Schematic representation of the PLS algorithm. The predictor matrix *X*, derived from XRD data, and the response matrix *Y*, based on the double-integrated EPR signal area for each sample, are decomposed into scores (*T* and *U*) and loadings (*P* and *Q*), with residuals represented by *E* and *F*, respectively.

Both of these poor outcomes are primarily attributable to the inherent noise in Raman spectral measurements, which adversely impacts the modeling accuracy and predictive performance, even though the PCA of the Raman spectral data revealed discernible clustering trends corresponding to varying concentration levels (Tables S6, S7 and Fig. S16, S17), exhibiting superior separation and data differentiation relative to the XRD measurements. So, regarding multivariate data analysis, Raman data seem to be better explained by exploratory or classification models, whereas XRD and EPR are more well-suited for calibration in this case.

These results, which indicate a correlation between the concentration of hexagonal phases and the density of point defects, contradict some previously reported experimental findings. However, they are supported by theoretical calculations. Many-body perturbation theory using the GW approximation,[95] along with density functional theory (DFT), has predicted that the studied defects are metastable in 3C-SiC and exhibit lower formation energies in hexagonal polytypes.[96] This implies that higher concentrations of hexagonal phases should indeed lead to an increased concentration of vacancies.

The EPR data were also simulated with known paramagnetic defects, carbon antisite vacancy – CAV, silicon vacancy – V_{Si}^{-}, and carbon vacancy – V_{C}^{+} using the EasySpin toolbox[59] (Fig. 5b–d and Fig. S10b–d, S11). Interestingly, while the total defect concentration showed no significant outliers, the changes in the individual defect concentrations demonstrated outlier behavior of the samples milled for two hours, similar to the Raman spectra. It was most obvious in the CAV concentration dependence on Al concentrations, as it is increasing with Al concentration for most of the samples, except for the one milled for two hours, but there is a remarkable difference in the case of V_{Si}^{-}, too. The maximum contribution of V_{Si}^{-} – approximately 5.05×10^{17} spins per cm^3, corresponding to ~35% relative contribution – was achieved through chemical synthesis by incorporating 10 mol% Al in the precursor and applying a two-hour milling process. This concentration is an order of magnitude higher than that obtained *via* the optimized irradiation technique[97] and even higher than most other reports,[98,99] demonstrating that the chemical route can yield V_{Si}^{-} centers in quantities comparable to, or even higher than, those produced by conventional methods.

The generation of negatively charged V_{Si}^{-} requires the coexistence of positively charged defects to satisfy charge neutrality. These are typically carbon vacancies, V_{C}^{+} or ionized N^{+} donors.[44,100–105] In irradiated samples, carbon vacancies are known to form more readily than silicon vacancies due to their lower formation energies and higher mobility,[44,105] often resulting in V_{C}^{+}/V_{Si}^{-} ratios $>3:1$. This excess of V_{C}^{+} can degrade spin coherence in ensemble-based quantum applications by introducing fluctuating charge and spin noise near V_{Si}^{-} centers.[100,106] In our chemically synthesized samples, the best-performing material yields a significantly improved V_{C}^{+}/V_{Si}^{-} ratios (3 : 2.1) compared to irradiated materials, which might be improved further as discussed in the next section.

The photoluminescence spectra of the samples under 520 nm excitation are shown in Fig. S12. All samples exhibited a broad luminescence signal that was deconvoluted (Fig. S13) into three components with peak centers at 1.90, 1.56, and 1.38 eV (650, 795, 900 nm). The center of the narrow peak at 1.38 eV (900 nm) is close to the emission line of the V_{Si}^{-} in hexagonal SiC at room temperature.[48,100,101] The intensity of this peak as a function of Al concentration in the precursor for various milling times is plotted in Fig. 7a and its spin concentration calculated *via* the EPR is in Fig. 7b. Although the PL intensities did not directly correlate with the V_{Si}^{-} concentrations determined by EPR, both measurements reached maximum values in the SiC10Al-2 h sample. This result is particularly promising considering the relatively low concentration of structural defects observed in samples milled for 2 hours. It should

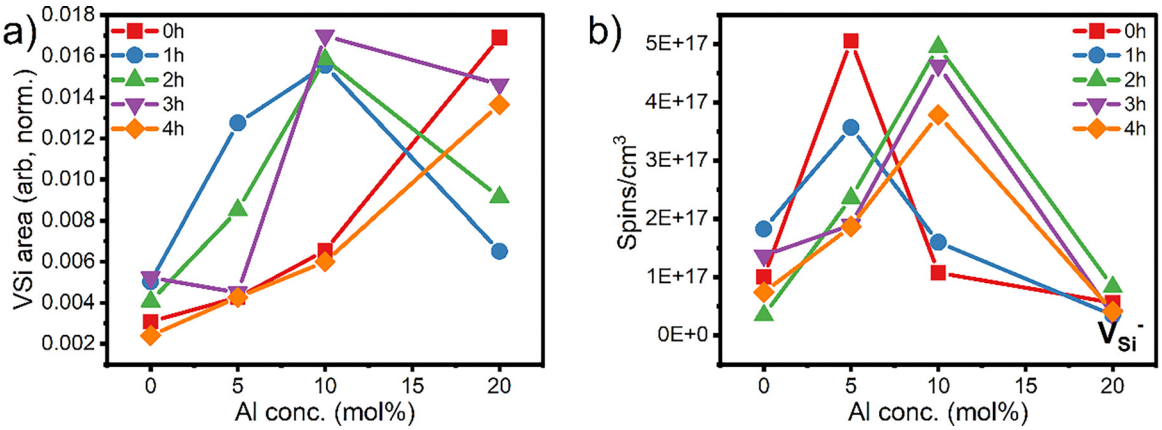

Fig. 7 (a) Results from the area of the PL measurement of samples and (b) V_{Si}^{-} spins per cm^3 after fitting with EasySpin.

be noted that the intensity of the photoemission is often influenced by extrinsic factors, such as the refractive index, particle shape, and the presence of other defects, which can compete in the photon absorption and emission processes. V_C^+, for example, is known for its quenching efficiency.[107]

3.1 The effect of aluminum on SiC formation

Our results demonstrate that both milling time and aluminum concentration significantly influence the final structural and defect properties of SiC, enabling optimization for specific applications. Based on comprehensive XRD, Raman, EPR, and PL data, we propose a reaction mechanism for defect formation and polytype evolution during synthesis.

The mechanism begins with the formation of aluminum carbide (1), as reported by Du *et al.*[108] followed by its reaction with elemental silicon (2). Both reactions exhibit negative Gibbs free energy, ΔG^0, values,[108] indicating thermodynamic favorability under the applied conditions.

$$3C_{(s)} + 4Al_{(l)} \rightarrow Al_4C_{3(s)} \quad (1)$$

$$Al_4C_{3(s)} + 3Si_{(l)} \rightarrow 3SiC_{(s)} + 4Al_{(l)} \quad (2)$$

This reaction pathway results in a carbon-deficient environment, which promotes the formation of carbon vacancies consistent with previous reports[109] and our EPR results.

The observed increase in antisite-vacancy complexes with higher Al concentrations in the precursor can be attributed to their stabilization under p-type conditions and the relatively low formation energies of these defects.[110,111] This p-type environment arises because a portion of the aluminum introduced as a precursor becomes incorporated into the SiC lattice during synthesis, acting as an acceptor dopant. Moreover, the migration of antisite vacancies toward silicon or carbon vacancies is thermally activated[112] above 1500 K. The photoluminescence data are consistent with the occurrence of primarily carbon antisite-vacancy pairs and silicon vacancies. However, carbon vacancies do not appear within the range where theoretical models suggest a zero phonon line (ZPL), between 1400 and 1900 nm.[113]

While the prevalence of the cubic 3C-SiC polytype in the non-Al samples is consistent with expectations, its significantly enhanced presence in samples made with 20 mol% Al is unexpected. Similar observations have been reported using different synthetic methods[70] where high Al concentrations and a nitrogen atmosphere facilitated the formation of 2H-AlN, which acts as a structural template for 3C-SiC growth. Moreover, nitrogen and phosphorus are known to stabilize cubic polytypes during growth.[114,115] In our scenario, despite the absence of nitrogen or phosphorus, it is plausible that excess aluminum reacts with available carbon to form Al_4C_3, rendering the system silicon-rich and thus favoring 3C-SiC formation, consistent with earlier findings.[3,114] According to Vasiliauskas *et al.*,[11] the transformation from 6H to 3C polytype can occur when stacking faults (SFs) develop in the 6H structure during growth. These faults disrupt the continuation of hexagonal stacking, enabling the nucleation and stabilization of the cubic phase, which is energetically favorable. It has been shown that the addition of aluminum enhances the formation of stacking faults in SiC,[55] which supports our proposed mechanism. Our XRD measurements confirm the presence of stacking faults, evidenced by a shoulder near the (111) reflection, while the Raman spectra independently corroborate the structural disorder consistent with SFs.

In addition to the thermodynamic and structural factors discussed above, defect formation is also governed by charge compensation. The generation of negatively charged vacancies requires the coexistence of positively charged defects to satisfy charge neutrality. Adjusting the Si : C stoichiometry in the precursor could offer a route to further reduce carbon vacancy concentrations and favor the formation of spin-active V_{Si}^{-}. However, for high silicon vacancy concentration, it is necessary to create compensating positive charges. Introducing nitrogen either through controlled atmospheres or additives could serve as an alternative charge compensation mechanism, as nitrogen donors are spinless in their ionized form (N^+) and can stabilize V_{Si}^{-} without contributing additional spin noise.

4. Conclusion

This study demonstrates that both aluminum concentration and milling time are critical parameters governing the

structural evolution and defect formation in SiC nanoparticles. An increase in Al content and a prolonged milling time facilitate the formation of hexagonal polytypes and significantly affect the generation of point defects. However, the influence of Al is concentration-dependent and becomes negligible above 20% Al in the precursor mixture. At or above this threshold, the reaction environment resembles that of the Al-free system, albeit with a reduced reaction temperature.

Statistical analysis reveals that defect concentration correlates more strongly with stacking fault density than with crystallite size, thereby challenging previous assumptions that primarily attributed defect formation to nanostructure dimensions. A notable finding from the comprehensive statistical evaluation is that, despite apparent visual and logical associations, no statistically significant correlation could be established between polytypism and crystallite size. Raman spectroscopy emerges as a promising complementary technique to XRD for structural analysis. However, to enable reliable correlation studies, a signal-to-noise ratio comparable to that of XRD is essential.

Quantification of defects *via* EPR shows that Al concentration and milling time can be tuned to achieve V_{Si}^{-} concentrations comparable to those obtained through irradiation-based methods. Among all conditions tested, 2-hour milling consistently yields the lowest structural disorder. The sample with 10% Al milled for 2 hours emerges as a promising candidate for the direct synthesis of color centers in SiC, exhibiting the highest concentration of V_{Si}^{-}. For applications targeting high concentrations of CAV, 2-hour milling without Al is most effective. In contrast, minimizing V_C^{+}, requires longer milling durations (3–4 hours) combined with elevated Al concentrations.

Finally, the high density of V_C^{+} and CAV, defects in the synthesized material, offers opportunities for post-synthetic tuning through thermal annealing. Vacancy migration at reduced temperatures—facilitated by the small crystallite sizes—may enable the formation of more complex and application-relevant defects, such as infrared-active divacancies.[112]

Author contributions

Sarah Morais Bezerra: investigation, formal analysis, methodology, writing – original draft, and visualization. Sándor Kollarics: methodology, validation, formal analysis, and writing – review & editing. Luisa Souza Almeida: methodology, formal analysis, validation, and writing – review & editing. Gábor Bortel: methodology, software, investigation, formal analysis, and writing – review & editing. Nikoletta Jegenyes: investigation, formal analysis, and writing – review & editing. Bence Gábor Márkus: methodology, validation, formal analysis, and writing – review & editing. Ferenc Simon: methodology, validation, formal analysis, writing – review & editing, and funding acquisition. Adam Gali: funding acquisition, supervision, conceptualization, writing – review & editing, and resources. David Beke: conceptualization, methodology, validation, data curation, writing – review & editing, supervision, and project administration.

Conflicts of interest

There are no conflicts to declare.

Data availability

The data supporting this article have been included as part of the supplementary information (SI). Supplementary information is available. See DOI: https://doi.org/10.1039/d5ma00751h.

Acknowledgements

This work was supported by the National Research, Development and Innovation Office of Hungary (NKFIH) and by the Ministry of Culture and Innovation Grants no. K137852, 149457, 2022-2.1.1-NL-2022-00004, TKP2021-NVA-02, and TKP2021-NVA-04. Luísa Souza Almeida thanks the Conselho Nacional de Desenvolvimento Científico e Tecnológico-CNPq scholarship (141537/2021-3).

References

1 S. Llmpijumnong and W. R. L. Lambrecht, Total Energy Differences Between Silicon Carbide Polytypes and their Implications for Crystal Growth, *MRS Proc.*, 1997, **492**, 145.
2 R. Maboudian, C. Carraro, D. G. Senesky and C. S. Roper, Advances in silicon carbide science and technology at the micro- and nanoscales, *J. Vac. Sci. Technol., A*, 2013, **31**(5), 050805.
3 N. W. Jepps and T. F. Page, Polytypic transformations in silicon carbide, *Prog. Cryst. Growth Charact.*, 1983, **7**(1–4), 259–307.
4 H. Abderrazak and E. S. B. Hadj Hmi, Silicon Carbide: Synthesis and Properties, in *Properties and Applications of Silicon Carbide*, ed. R. Gerhardt, InTech, 2011.
5 A. L. Falk, B. B. Buckley, G. Calusine, W. F. Koehl, V. V. Dobrovitski, A. Politi, C. A. Zorman, P. X.-L. Feng and D. D. Awschalom, Polytype control of spin qubits in silicon carbide, *Nat. Commun.*, 2013, **4**, 1819.
6 A. S. Mukasyan, Y.-C. Lin, A. S. Rogachev and D. O. Moskovskikh, Direct Combustion Synthesis of Silicon Carbide Nanopowder from the Elements, *J. Am. Ceram. Soc.*, 2013, **96**(1), 111–117.
7 W. F. Knippenberg, Growth phenomena in silicon carbide, *Philips Res. Rep.*, 1963, **18**, 161–274.
8 Y. Inomata, A. Inoue, M. Mitomo and H. Suzuki, *Relation between growth temperature and the structure of SiC crystals grown by the sublimation method*. Air Force Cambridge Research Laboratories, United States Air Force, 1969, **62**.
9 R. Yakimova, M. Syväjärvi, T. Iakimov, H. Jacobsson, R. Råback, A. Vehanen and E. Janzén, Polytype stability

in seeded sublimation growth of 4H-SiC boules, *J. Cryst. Growth*, 2000, **217**(3), 255–262.
10 V. Heine, C. Cheng and R. J. Needs, The Preference of Silicon Carbide for Growth in the Metastable Cubic Form, *J. Am. Ceram. Soc.*, 1991, **74**(10), 2630–2633.
11 R. Vasiliauskas, M. Marinova, M. Syväjärvi, E. K. Polychroniadis and R. Yakimova, Polytype transformation and structural characteristics of 3C-SiC on 6H-SiC substrates, *J. Cryst. Growth*, 2014, **395**, 109–115.
12 P. Raj, G. S. Gupta and V. Rudolph, Silicon carbide formation by carbothermal reduction in the Acheson process: a hot model study, *Thermochim. Acta*, 2020, **687**, 178577.
13 P. V. Kumar and G. S. Gupta, Study of formation of silicon carbide in the Acheson process, *Steel Res.*, 2002, **73**(2), 31–38.
14 V. D. Heydemann, N. Schulze, D. L. Barrett and G. Pensl, Growth of 6H and 4H silicon carbide single crystals by the modified Lely process utilizing a dual-seed crystal method, *Appl. Phys. Lett.*, 1996, **69**(24), 3728–3730.
15 J. Lee, D. Kim, D. Shin, H.-G. Lee, J. Y. Park and W.-J. Kim, A new process for minimizing residual silicon and carbon of reaction-bonded silicon carbide via chemical vapor deposition, *J. Eur. Ceram. Soc.*, 2021, **41**(7), 4000–4005.
16 L. N. Satapathy, P. D. Ramesh, D. Agrawal and R. Roy, Microwave synthesis of phase-pure, fine silicon carbide powder, *Mater. Res. Bull.*, 2005, **40**(10), 1871–1882.
17 Y. Yang, Z. Tong, X. Pi, D. Yang and Y. Huang, Advances and challenges in 4H silicon carbide: defects and impurities, *Phys. Scr.*, 2024, **99**(9), 092001.
18 A. Kar, K. Kundu, S. Kumar, R. Banerjee and H. Chattopadhyay, Synthesis of silicon carbide thin film as a source for white light emission, *Opt. Mater.*, 2024, **155**, 115795.
19 A. S. Mukasyan, Y. Lin, A. S. Rogachev and D. O. Moskovskikh, Direct Combustion Synthesis of Silicon Carbide Nanopowder from the Elements, *J. Am. Ceram. Soc.*, 2013, **96**(1), 111–117.
20 Y. Yang, Z.-M. Lin and J.-T. Li, Synthesis of SiC by silicon and carbon combustion in air, *J. Eur. Ceram. Soc.*, 2009, **29**(1), 175–180.
21 J. J. Moore and H. J. Feng, Combustion synthesis of advanced materials: Part I. Reaction parameters, *Prog. Mater. Sci.*, 1995, **39**(4–5), 243–273.
22 G. Liu, J. Li and K. Chen, Combustion Synthesis, *Handbook of Combustion*, Wiley, 1 edn, 2016, pp. 1–62.
23 E. Schmitt, T. Straubinger, M. Rasp, M. Vogel and A. Wohlfart, Polytype stability and defects in differently doped bulk SiC, *J. Cryst. Growth*, 2008, **310**(5), 966–970.
24 T. Shiramomo, B. Gao, F. Mercier, S. Nishizawa, S. Nakano and K. Kakimoto, Study of the effect of doped impurities on polytype stability during PVT growth of SiC using 2D nucleation theory, *J. Cryst. Growth*, 2014, **385**, 95–99.
25 C. Jacquier, D. Chaussende, G. Ferro, J. C. Viala, F. Cauwet and Y. Monteil, Study of the interaction between graphite and Al–Si melts for the growth of crystalline silicon carbide, *J. Mater. Sci.*, 2002, **37**(15), 3299–3306.
26 Z. Rajabzadeh, R. Hammer and L. Romaner, On the impact of nitrogen and aluminum doping on silicon carbide polytype stability: insights from first principle calculations, *J. Am. Ceram. Soc.*, 2025, **108**(4), e20284.
27 L. Lai, Y. Cui, Y. Zhong, K. Y. Cheong, H. Linewih, X. Xu and J. Han, Impacts of silicon carbide defects on electrical characteristics of SiC devices, *J. Appl. Phys.*, 2025, **137**(6), 060701.
28 T. Plakhotnik and H. Aman, NV-centers in nanodiamonds: How good they are, *Diamond Related Mater.*, 2018, **82**, 87–95.
29 J. M. Abendroth, K. Herb, E. Janitz, T. Zhu, L. A. Völker and C. L. Degen, Single-Nitrogen–Vacancy NMR of Amine-Functionalized Diamond Surfaces, *Nano Lett.*, 2022, **22**(18), 7294–7303.
30 D. D. Awschalom, R. Epstein and R. Hanson, The Diamond Age Diamond Age of Spintronics, *Sci. Am.*, 2007, **297**(4), 84–91.
31 M. W. Doherty, N. B. Manson, P. Delaney, F. Jelezko, J. Wrachtrup and L. C. L. Hollenberg, The nitrogen-vacancy colour centre in diamond, *Phys. Rep.*, 2013, **528**(1), 1–45.
32 S. G. Carter, Ö. O. Soykal, P. Dev, S. E. Economou and E. R. Glaser, Spin coherence and echo modulation of the silicon vacancy in 4H-SiC at room temperature, *Phys. Rev. B: Condens. Matter Mater. Phys.*, 2015, **92**(16), 161202.
33 L. Latypova, F. Murzakhanov, G. Mamin, M. Sadovnikova, H. J. Von Bardeleben, J. V. Rau and M. Gafurov, Exploring High-Spin Color Centers in Wide Band Gap Semiconductors SiC: A Comprehensive Magnetic Resonance Investigation (EPR and ENDOR Analysis), *Molecules*, 2024, **29**(13), 3033.
34 G. Andrini, F. Amanti, F. Armani, V. Bellani, V. Bonaiuto, S. Cammarata, M. Campostrini, T. H. Dao, F. De Matteis, V. Demontis, G. Di Giuseppe, S. Ditalia Tchernij, S. Donati, A. Fontana, J. Forneris, R. Francini, L. Frontini, R. Gunnella, S. Iadanza, A. E. Kaplan, C. Lacava, V. Liberali, F. Marzioni, E. Nieto Hernández, E. Pedreschi, P. Piergentili, D. Prete, P. Prosposito, V. Rigato, C. Roncolato, F. Rossella, A. Salamon, M. Salvato, F. Sargeni, J. Shojaii, F. Spinella, A. Stabile, A. Toncelli, G. Trucco and V. Vitali, Solid-State Color Centers for Single-Photon Generation, *Photonics*, 2024, **11**(2), 188.
35 S. Castelletto and A. Boretti, Silicon carbide color centers for quantum applications, *J. Phys. Photonics*, 2020, **2**(2), 022001.
36 M. Alhabeb, K. Maleski, B. Anasori, P. Lelyukh, L. Clark, S. Sin and Y. Gogotsi, Guidelines for Synthesis and Processing of Two-Dimensional Titanium Carbide ($Ti_3C_2T_i$ MXene), *Chem. Mater.*, 2017, **29**(18), 7633–7644.
37 W. F. Koehl, B. B. Buckley, F. J. Heremans, G. Calusine and D. D. Awschalom, Room temperature coherent control of defect spin qubits in silicon carbide, *Nature*, 2011, **479**(7371), 84–87.
38 G. Pacchioni, Spin qubits: useful defects in silicon carbide, *Nat. Rev. Mater.*, 2017, **2**(8), 17052.
39 S. Majety, P. Saha, V. A. Norman and M. Radulaski, Quantum information processing with integrated silicon carbide photonics, *J. Appl. Phys.*, 2022, **131**(13), 130901.

40 K. Tahara, S. Tamura, H. Toyama, J. J. Nakane, K. Kutsuki, Y. Yamazaki and T. Ohshima, Quantum sensing with duplex qubits of silicon vacancy centers in SiC at room temperature, *npj Quantum Inf*, 2025, **11**(1), 58.
41 A. Yi, C. Wang, L. Zhou, Y. Zhu, S. Zhang, T. You, J. Zhang and X. Ou, Silicon carbide for integrated photonics, *Appl. Phys. Rev.*, 2022, **9**(3), 031302.
42 H. Kraus, V. A. Soltamov, D. Riedel, S. Väth, F. Fuchs, A. Sperlich, P. G. Baranov, V. Dyakonov and G. V. Astakhov, Room-temperature quantum microwave emitters based on spin defects in silicon carbide, *Nat. Phys.*, 2014, **10**(2), 157–162.
43 S. Castelletto and A. Boretti, Silicon carbide color centers for quantum applications, *J. Phys. Photonics*, 2020, **2**(2), 022001.
44 C. Zhang, F. Gygi and G. Galli, Engineering the formation of spin-defects from first principles, *Nat. Commun.*, 2023, **14**(1), 5985.
45 A. L. Falk, B. B. Buckley, G. Calusine, W. F. Koehl, V. V. Dobrovitski, A. Politi, C. A. Zorman, P. X.-L. Feng and D. D. Awschalom, Polytype control of spin qubits in silicon carbide, *Nat. Commun.*, 2013, **4**(1), 1819.
46 S. Pezzagna and J. Meijer, Quantum computer based on color centers in diamond, *Appl. Phys. Rev.*, 2021, **8**(1), 011308.
47 N. Mizuochi and N. Morioka, Quantum light sources based on color centers in diamond and silicon carbide, in *Quantum Photonics*, ed. Y. Arakawa and D. Bimberg, Elsevier, 2024, ch. 7, pp. 339–368.
48 C. Chen, B. Jiang and X. Hu, Research Progress on Silicon Vacancy Color Centers in Diamond, *Funct. Diamond*, 2024, **4**(1), 2332346.
49 Z. Ju, J. Lin, S. Shen, B. Wu and E. Wu, Preparations and applications of single color centers in diamond, *Adv. Phys.: X*, 2021, **6**(1), 1858721.
50 S. Castelletto and A. Boretti, Silicon carbide color centers for quantum applications, *J. Phys. Photonics*, 2020, **2**(2), 022001.
51 G. Thiering and A. Gali, Color centers in diamond for quantum applications, *Semiconductors and Semimetals*, Elsevier, 2020, vol. 103, pp. 1–36.
52 J. O. Orwa, A. D. Greentree, I. Aharonovich, A. D. C. Alves, J. Van Donkelaar, A. Stacey and S. Prawer, Fabrication of single optical centres in diamond—a review, *J. Lumin.*, 2010, **130**(9), 1646–1654.
53 A. Csóré, N. Mukesh, G. Károlyházy, D. Beke and A. Gali, Photoluminescence spectrum of divacancy in porous and nanocrystalline cubic silicon carbide, *J. Appl. Phys.*, 2022, **131**(7), 071102.
54 N. Mukesh, B. G. Márkus, N. Jegenyes, G. Bortel, S. M. Bezerra, F. Simon, D. Beke and A. Gali, Formation of Paramagnetic Defects in the Synthesis of Silicon Carbide, *Micromachines*, 2023, **14**(8), 1517.
55 D. Beke, J. Valenta, G. Károlyházy, S. Lenk, Z. Czigány, B. G. Márkus, K. Kamarás, F. Simon and A. Gali, Room-Temperature Defect Qubits in Ultrasmall Nanocrystals, *J. Phys. Chem. Lett.*, 2020, **11**(5), 1675–1681.
56 D. Beke, A. Fučíková, T. Z. Jánosi, G. Károlyházy, B. Somogyi, S. Lenk, O. Krafcsik, Z. Czigány, J. Erostyák, K. Kamarás, J. Valenta and A. Gali, Direct Observation of Transition from Solid-State to Molecular-Like Optical Properties in Ultrasmall Silicon Carbide Nanoparticles, *J. Phys. Chem. C*, 2018, **122**(46), 26713–26721.
57 D. Beke, G. Károlyházy, Z. Czigány, G. Bortel, K. Kamarás and A. Gali, Harnessing no-photon exciton generation chemistry to engineer semiconductor nanostructures, *Sci. Rep.*, 2017, **7**(1), 10599.
58 S. M. Bezerra, G. Bortel, N. Jegenyes, A. Gali and D. Beke, Aluminium-induced modulation of reaction kinetics and polytype formation in silicon carbide synthesized through high-energy ball milling, *Materialia*, 2025, **39**, 102357.
59 S. Stoll and A. Schweiger, EasySpin, a comprehensive software package for spectral simulation and analysis in EPR, *J. Magn. Reson.*, 2006, **178**(1), 42–55.
60 D. Ballabio, A MATLAB toolbox for Principal Component Analysis and unsupervised exploration of data structure, *Chemom. Intell. Lab. Syst.*, 2015, **149**, 1–9.
61 V. Consonni, G. Baccolo, F. Gosetti, R. Todeschini and D. Ballabio, A MATLAB toolbox for multivariate regression coupled with variable selection, *Chemom. Intell. Lab. Syst.*, 2021, **213**, 104313.
62 D. Shillan, J. A. C. Sterne, A. Champneys and B. Gibbison, Use of machine learning to analyse routinely collected intensive care unit data: a systematic review, *Crit Care*, 2019, **23**(1), 284.
63 P. Lapadula, G. Mecca, D. Santoro, L. Solimando and E. Veltri, Greg, ML – Machine Learning for Healthcare at a Scale, *Health Technol.*, 2020, **10**(6), 1485–1495.
64 S. Wold, Chemometrics; what do we mean with it, and what do we want from it?, *Chemom. Intell. Lab. Syst.*, 1995, **30**(1), 109–115.
65 Y. Xing, B. Ren, B. Li, J. Chen, S. Yin, H. Lin and Y. Liu, Synthesis of sub-micron sized SiC particles with high defect density by using polytetrafluoroethylene as an additive, *Int J. Appl. Ceram. Technol.*, 2024, **21**(6), 3886–3896.
66 K. Sun, T. Wang, W. Gong, W. Lu, X. He, E. G. Eddings and M. Fan, Synthesis and potential applications of silicon carbide nanomaterials/nanocomposites, *Ceram. Int.*, 2022, **48**(22), 32571–32587.
67 T. Yoshikawa, K. Morita, S. Kawanishi and T. Tanaka, Thermodynamics of impurity elements in solid silicon, *J. Alloys Compd.*, 2010, **490**(1–2), 31–41.
68 H. Kodera, Diffusion Coefficients of Impurities in Silicon Melt, *Jpn. J. Appl. Phys.*, 1963, **2**(4), 212.
69 H. Ghezelbash, A. Zeinali, N. Ehsani and H. R. Baharvandi, The effect of aluminum additive on pressureless sintering of SiC, *J. Aust. Ceram. Soc.*, 2019, **55**(4), 903–911.
70 J. Hvam, P. Morgen, E. M. Skou, U. G. Nielsen, T. Wolff and T. E. Warner, The role of aluminium as an additive element in the synthesis of porous 4H-silicon carbide, *J. Eur. Ceram. Soc.*, 2016, **36**(14), 3267–3278.

71 M. Wieligor, Y. Wang and T. W. Zerda, Raman spectra of silicon carbide small particles and nanowires, *J. Phys.: Condens. Matter*, 2005, **17**(15), 2387.
72 M. Makowska-Janusik, A. Kassiba, J. Bouclé, J.-F. Bardeau, S. Kodjikian and A. Désert, Vibrational density of states in silicon carbide nanoparticles: experiments and numerical simulations, *J. Phys.: Condens. Matter*, 2005, **17**(33), 5101.
73 S. Rohmfeld, M. Hundhausen and L. Ley, Raman scattering in polycrystalline 3C-SiC: influence of stacking faults, *Phys. Rev. B: Condens. Matter Mater. Phys.*, 1998, **58**(15), 9858–9862.
74 G. Chikvaidze, N. Mironova-Ulmane, A. Plaude and O. Sergeev, Investigation of Silicon Carbide Polytypes by Raman Spectroscopy, *Latv. J. Phys. Tech. Sci.*, 2014, **51**(3), 51–57.
75 J. Wasyluk, T. S. Perova, S. A. Kukushkin, A. V. Osipov, N. A. Feoktistov and S. A. Grudinkin, Raman Investigation of Different Polytypes in SiC Thin Films Grown by Solid-Gas Phase Epitaxy on Si(111) and 6H-SiC Substrates, *Mater. Sci. Forum*, 2010, **645–648**, 359–362.
76 S. Nakashima, T. Mitani, M. Tomobe, T. Kato and H. Okumura, Raman characterization of damaged layers of 4H-SiC induced by scratching, *AIP Adv.*, 2016, **6**(1), 015207.
77 M. Wieligor, R. Rich and T. W. Zerda, Study on silicon carbide nanowires produced from carbon blacks and structure of carbon blacks, *J. Mater. Sci.*, 2010, **45**(7), 1725–1733.
78 P. F. Wang, L. Huang, W. Zhu and Y. F. Ruan, Raman scattering of neutron irradiated 6H-SiC, *Solid State Commun.*, 2012, **152**(10), 887–890.
79 P. Wang and S. Wang, Raman Scattering Study of Silicon Carbide Irradiated with 1.25 MeV Si Ions, *IOP Conf. Ser.: Mater. Sci. Eng.*, 2019, **493**(1), 012092.
80 G. Roma, Linear response calculation of first-order Raman spectra of point defects in silicon carbide, *Phys. Status Solidi A*, 2016, **213**(11), 2995–2999.
81 G. Roma, Linear response calculation of first-order Raman spectra of point defects in silicon carbide, *Phys. Status Solidi A*, 2016, **213**(11), 2995–2999.
82 S. Nakashima and H. Harima, Raman Investigation of SiC Polytypes, *Phys. Status Solidi A*, 1997, **162**(1), 39–64.
83 L. B. Bayu Aji, E. Stavrou, J. B. Wallace, A. Boulle, A. Debelle and S. O. Kucheyev, Comparative study of radiation defect dynamics in 3C-SiC by X-ray diffraction, Raman scattering, and ion channeling, *Appl. Phys. A*, 2019, **125**(1), 28.
84 S. P. Singh, R. P. S. Chakradhar, J. L. Rao and B. Karmakar, EPR, FTIR, optical absorption and photoluminescence studies of Fe_2O_3 and CeO_2 doped ZnO–Bi_2O_3–B_2O_3 glasses, *J. Alloys Compd.*, 2010, **493**(1–2), 256–262.
85 N. K. D. A. M. Galvão, G. D. Vasconcelos, M. V. R. D. Santos, T. M. B. Campos, R. S. Pessoa, M. Guerino, M. A. Djouadi and H. S. Maciel, Growth and Characterization of Graphene on Polycrystalline SiC Substrate Using Heating by CO_2 Laser Beam, *Mat. Res.*, 2016, **19**(6), 1329–1334.
86 N. Swaminathan, P. J. Kamenski, D. Morgan and I. Szlufarska, Effects of grain size and grain boundaries on defect production in nanocrystalline 3C-SiC, *Acta Mater.*, 2010, **58**(8), 2843–2853.
87 G. Cheng, T.-H. Chang, Q. Qin, H. Huang and Y. Zhu, Mechanical Properties of Silicon Carbide Nanowires: Effect of Size-Dependent Defect Density, *Nano Lett.*, 2014, **14**(2), 754–758.
88 F. La Via, M. Camarda and A. La Magna, Mechanisms of growth and defect properties of epitaxial SiC, *Appl. Phys. Rev.*, 2014, **1**(3), 031301.
89 A. Leth-Espensen, P. Glarborg and P. A. Jensen, Predicting Biomass Char Yield from High Heating Rate Devolatilization Using Chemometrics, *Energy Fuels*, 2018, **32**(9), 9572–9580.
90 L. Souza Almeida, I. Duarte Coutinho, A. J. Borim de Souza, L. A. Colnago and F. M. M. Ocampos, NMR-based Metabolomics for Plant Biomass Analysis, *Analytical Techniques and Methods for Biomass*, 2025, vol. 2.
91 M. F. Pimentel, R. K. H. Galvão and M. C. U. D. Araújo, Recomendações para calibração em Química Analítica parte 2: calibração multianalito, *Quím. Nova*, 2008, **31**(2), 462–467.
92 T. Rajalahti and O. M. Kvalheim, Multivariate data analysis in pharmaceutics: a tutorial review, *Int. J. Pharm.*, 2011, **417**(1–2), 280–290.
93 C. B. Y. Cordella, The Basic Building Block of Chemometrics, in *Analytical Chemistry*, ed. I. S. Krull, InTech, 2012.
94 K. Kumar, Principal component analysis: most favourite tool in chemometrics, *Reson*, 2017, **22**(8), 747–759.
95 F. Bruneval and G. Roma, Energetics and metastability of the silicon vacancy in cubic SiC, *Phys. Rev. B: Condens. Matter Mater. Phys.*, 2011, **83**(14), 144116.
96 T. Ito, T. Kondo, T. Akiyama and K. Nakamura, Theoretical investigations of the polytypism in silicon carbide: contribution of the vacancy formation, *Phys. Status Solidi C*, 2011, **8**(2), 583–585.
97 C. Kasper, D. Klenkert, Z. Shang, D. Simin, A. Gottscholl, A. Sperlich, H. Kraus, C. Schneider, S. Zhou, M. Trupke, W. Kada, T. Ohshima, V. Dyakonov and G. V. Astakhov, Influence of Irradiation on Defect Spin Coherence in Silicon Carbide, *Phys. Rev. Appl.*, 2020, **13**(4), 044054.
98 A. A. Lebedev, G. A. Oganesyan, V. V. Kozlovski, I. A. Eliseyev and P. V. Bulat, Radiation Defects in Heterostructures 3C-SiC/4H-SiC, *Crystals*, 2019, **9**(2), 115.
99 C. Altana, L. Calcagno, C. Ciampi, F. La Via, G. Lanzalone, A. Muoio, G. Pasquali, D. Pellegrino, S. Puglia, G. Rapisarda and S. Tudisco, Radiation Damage by Heavy Ions in Silicon and Silicon Carbide Detectors, *Sensors*, 2023, **23**(14), 6522.
100 R. Nagy, M. Niethammer, M. Widmann, Y.-C. Chen, P. Udvarhelyi, C. Bonato, J. U. Hassan, R. Karhu, I. G. Ivanov, N. T. Son, J. R. Maze, T. Ohshima, Ö. O. Soykal, Á. Gali, S.-Y. Lee, F. Kaiser and J. Wrachtrup, High-fidelity spin and optical control of single silicon-vacancy centres in silicon carbide, *Nat. Commun.*, 2019, **10**(1), 1954.
101 T. Lingner, S. Greulich-Weber, J.-M. Spaeth, U. Gerstmann, E. Rauls, Z. Hajnal, T. Frauenheim and H. Overhof, Structure of the silicon vacancy in 6H-SiC after annealing

identified as the carbon vacancy–carbon antisite pair, *Phys. Rev. B: Condens. Matter Mater. Phys.*, 2001, **64**(24), 245212.
102 T. Kimoto, K. Kawahara, B. Zippelius, E. Saito and J. Suda, Control of carbon vacancy in SiC toward ultrahigh-voltage power devices, *Superlattices Microstruct.*, 2016, **99**, 151–157.
103 D. Liu, F. Kaiser, V. Bushmakin, E. Hesselmeier, T. Steidl, T. Ohshima, N. T. Son, J. Ul-Hassan, Ö. O. Soykal and J. Wrachtrup, The silicon vacancy centers in SiC: determination of intrinsic spin dynamics for integrated quantum photonics, *npj Quantum Inf*, 2024, **10**(1), 1–9.
104 M. E. Bathen, A. Galeckas, J. Müting, H. M. Ayedh, U. Grossner, J. Coutinho, Y. K. Frodason and L. Vines, Electrical charge state identification and control for the silicon vacancy in 4H-SiC, *npj Quantum Inf*, 2019, **5**(1), 1–9.
105 A. Scholle, S. Greulich-Weber, E. Rauls, W. G. Schmidt and U. Gerstmann, Vacancy clusters created via room temperature irradiation in 6H-SiC, *Phys. B*, 2009, **404**(23), 4742–4744.
106 E. M. Y. Lee, A. Yu, J. J. de Pablo and G. Galli, Stability and molecular pathways to the formation of spin defects in silicon carbide, *Nat. Commun.*, 2021, **12**(1), 6325.
107 S. Castelletto, Silicon carbide single-photon sources: challenges and prospects, *Mater. Quantum. Technol.*, 2021, **1**(2), 023001.
108 X. Du, T. Gao, D. Li, Y. Wu and X. Liu, A novel approach to synthesize SiC particles by in situ reaction in Al–Si–C alloys, *J. Alloys Compd.*, 2014, **588**, 374–377.
109 J.-I. Iwata, C. Shinei and A. Oshiyama, Density-functional study of atomic and electronic structures of multivacancies in silicon carbide, *Phys. Rev. B*, 2016, **93**(12), 125202.
110 P. A. Schultz, R. M. Van Ginhoven and A. H. Edwards, Theoretical study of intrinsic defects in cubic silicon carbide 3C-SiC, *Phys. Rev. B*, 2021, **103**(19), 195202.
111 F. Gao, W. J. Weber, H. Y. Xiao and X. T. Zu, Formation and properties of defects and small vacancy clusters in SiC: ab initio calculations, *Nucl. Instrum. Methods Phys. Res., Sect. B*, 2009, **267**(18), 2995–2998.
112 C. Zhang, F. Gygi and G. Galli, Engineering the formation of spin-defects from first principles, *Nat. Commun.*, 2023, **14**(1), 5985.
113 M. Mohseni, P. Udvarhelyi, G. Thiering and A. Gali, Positively charged carbon vacancy defect as a near-infrared emitter in 4H-SiC, *Phys. Rev. Mater.*, 2023, **7**(9), 096202.
114 T. F. Page, Silicon Carbide: Structure and Polytypic Transformations, in *The Physics and Chemistry of Carbides, Nitrides and Borides*, ed. R. Freer, Springer Netherlands, Dordrecht, 1990, pp. 197–214.
115 J. Lorenzzi, V. Souliere, D. Carole, N. Jegenyes, O. Kim-Hak, F. Cauwet and G. Ferro, Effect of nitrogen impurity on the stabilization of 3C-SiC polytype during heteroepitaxial growth by vapor–liquid–solid mechanism on 6H-SiC substrates, *Diamond Related Mater.*, 2011, **20**(5–6), 808–813.